



RESEARCH ARTICLE

10.1029/2022GC010796

Microscale Magnetic Inversion of Remanent Magnetization Mineral Sources From the Black Hill Norite, South Australia

M. D. Lee¹ , S. McEnroe¹ , Z. Pastore¹ , N. Church¹ , and P. Schmidt²¹Department of Geoscience and Petroleum, Norwegian University of Science and Technology, Trondheim, Norway,²Magnetic Earth, Sydney, Australia

Key Points:

- Scanning magnetic microscopy and microscale modeling are used to detect the occurrence of ferromagnetic phases in a paramagnetic host
- Microstructures such as lamellae result in anisotropic magnetic susceptibility, which plays a key contribution to bulk magnetic properties
- Inverse modeling of tabular bodies was efficient in quantifying local variation of the magnetization associated to microstructures

Supporting Information:

Supporting Information may be found in the online version of this article.

Correspondence to:

M. D. Lee,

Madeline.Lee@ntnu.no

Citation:

Lee, M. D., McEnroe, S., Pastore, Z., Church, N., & Schmidt, P. (2023). Microscale magnetic inversion of remanent magnetization mineral sources from the Black Hill Norite, South Australia. *Geochemistry, Geophysics, Geosystems*, 24, e2022GC010796. <https://doi.org/10.1029/2022GC010796>

Received 21 NOV 2022

Accepted 28 MAR 2023

Abstract Inverse modeling of regional-scale aeromagnetic data is complicated due to the non-uniqueness principle and interference of anomalies, especially with increased source-sensor separation. This is why in situ data and constraints are required to create a reliable inversion model. However, these complications even exist when analysis is conducted at a microscale level with the magnetic mapping of a thin section. Here, we assess the impact of magnetic minerals on adjacent non-magnetic minerals, specifically magnetite and ilmenite, respectively. The sample is from the Black Hill Norite, South Australia, which has been the focus of both paleomagnetic and geophysical modeling. Here, we conduct inverse modeling of all opaque minerals in the thin section. During post-modeling, the opaque minerals are identified as magnetite or ilmenite using backscatter electron imaging for quantifiable classification. The results show that ilmenite will exhibit a magnetic intensity and direction when magnetite lamellae are present or when it is adjacent to a magnetite grain from which the ilmenite grain was oxy-exsolved. We also assess the scale of interpretation by modeling the grains both as a singular volume (frustum) and as a series of smaller volumes (tabular arrays). It is shown that although the magnetic field generated by the frustums and the tabular arrays are quantitatively similar to the original measured magnetic field from the scanning magnetic microscope, the tabular array produces a closer fit to the modeled anomaly.

Plain Language Summary Magnetic anomalies are values that deviate from the baseline magnetic field and are due to the presence of a magnetic source, such as a rock or mineral. The anomaly of a magnetic mineral may influence measurements of adjacent non-magnetic minerals. If this impact is not considered, then false solutions may be overlooked in the interpretation and modeling process. Using a sample from the Black Hill Norite intrusion in South Australia, we show that the magnetic mineral, magnetite, impacts the results for the non-magnetic mineral, ilmenite, when completing 3D modeling. In this sample, when an ilmenite grain contains thin magnetite blades or is next to a magnetite grain, the modeled magnetic anomaly is controlled by the magnetite and not the ilmenite itself. In 3D modeling, grains are represented as a single large volume or numerous small volumes. The magnetic field produced by modeling solutions for both approaches is similar to the original measured field of the sample. However, when the magnetic field values are assessed along a profile, the smaller volumes result in a closer match to the laboratory-measured values.

1. Introduction

Aeromagnetic surveying maps the distribution of magnetic minerals, where the magnetic properties originate from opaque minerals, most commonly magnetite (Balsley, 1958; Grant, 1984). Interpretation of aeromagnetic anomalies requires inferences on geology. However, reliable interpretations may be hampered by disregarding what is occurring with the magnetic minerals at a microscale (Austin & Foss, 2014; Grant, 1984; McEnroe et al., 2009). Microscale magnetic mapping of thin sections is becoming more common with the development of scanning magnetic microscopy (SMM) (Church & McEnroe, 2018; Egli & Heller, 2000; Hankard et al., 2009; Oda et al., 2016; Pastore et al., 2021; Thomas et al., 1992; Weiss et al., 2000, 2007) and provides insight on small-scale variations that in summation contribute to anomalies mapped at regional scales. In aeromagnetic interpretation, the magnetic anomaly is largely influenced by both the depth and volume of the source, and its intensity and direction of magnetization (Bhattacharyya, 1966; Phillips, 2005; Roest et al., 1992; Spector & Grant, 1970). In magnetic mapping of thin sections, the resultant mapped anomalies will be strongly influenced by the volume of the source and direction of magnetization due to thickness on the scale of microns from sample preparation. In a recent work, Pastore et al. (2022) show that the inversion of SMM data can also be used on mm-thick sample slices by jointly modeling the magnetic data measured above and below the sample slice.

© 2023. The Authors. *Geochemistry, Geophysics, Geosystems* published by Wiley Periodicals LLC on behalf of American Geophysical Union. This is an open access article under the terms of the [Creative Commons Attribution-NonCommercial-NoDerivs License](https://creativecommons.org/licenses/by/4.0/), which permits use and distribution in any medium, provided the original work is properly cited, the use is non-commercial and no modifications or adaptations are made.

Traditionally, magnetic modeling assumes that the region of interpretation consists of independent rectangular, vertical-sided parallelepipeds. The anomalies generated by these magnetic blocks may intersect one another depending on the geometry of the anomaly and proximity to other nearby magnetic blocks (Spector & Grant, 1970). Separating the contributions of different blocks is important for reliable magnetic and geological modeling. Magnetic anomaly interference is well studied on regional geological models because it can diminish the reliability of common interpretation methodologies that rely on discrete magnetic sources. There has been, however, limited analysis made on magnetic anomaly interference at the microscopic level.

Here, we demonstrate that inversion solutions for discrete paramagnetic ilmenite grains in a thin section are affected by adjacent magnetite grains from which the ilmenite lamellae were oxy-exsolved or by magnetite lamellae formed by reduction-exsolution from ilmenite grains. Synthetic studies on the magnetic implications of lamellae have been conducted because the anisotropic magnetic susceptibility of lamellae will affect both the shape and amplitude of magnetic anomalies (Biedermann & McEnroe, 2017). This is particularly important when oxide lamellae with a strong crystallographic preferred orientation are abundant (Robinson, Heidelbach et al., 2006; Robinson et al., 2002, 2013, 2016). Here, magnetism may be strongest when: (a) the proportion of exsolved lamellae material is large, (b) the total area of the exsolution interfaces is large, and (c) host planes are parallel to the magnetizing field (Robinson, Harrison, & McEnroe, 2006; Robinson et al., 2013, 2021). Grain size is also a crucial factor influencing magnetization, especially of titanomagnetite-bearing rocks (Clark, 1997; Dunlop, 1981).

Here, SMM is first implemented in near field free conditions to map magnetic anomalies due to the presence of remanent magnetization. Analogous to aeromagnetic surveys in which anomalies are deviations from a geomagnetic or planetary baseline field, anomalies in remanence SMM measurements reflect deviations from a zero-field baseline. Using this SMM anomaly map, we conduct inversion modeling to estimate the remanent magnetic intensity and direction (declination, inclination). Through analysis of stereonet and rose diagrams, we identify populations of grains with different magnetization directions. Shape anisotropy from magnetite lamellae within ilmenite grains (Robinson et al., 2016) is a principal factor contributing to the magnetic fingerprint of identified populations. A profile and statistical comparison of model geometry addresses how bulk magnetic characteristics (frustum) versus small-scale variations (tabular) may impact model interpretation. A discussion on inversion modeling using different source volume discretization and model design, frustum versus tabular, is presented along with the potential artifacts.

2. Geology and Geophysics of Study Area

The Black Hill Norite (BHN) is a poorly exposed mafic intrusion and is one of three plutons within the Black Hill Complex, which intruded during the Ordovician period approximately 487 ± 5 Ma ago (Brown et al., 1988; Rajagopalan et al., 1993, 1995; Schmidt et al., 1993). The norite is important because it has yielded an Early Ordovician paleomagnetic pole position for Australia (Rajagopalan et al., 1993; Schmidt et al., 1993). The paleomagnetic measurements from the BHN exhibit an intensity and direction different from the local magnetic inclination and declination due to strong and stable NRM (Foss & McKenzie, 2011; Pratt et al., 2012). Previous work assumed the remanence to be thermal in origin and carried by fine-grained single- (SD) or pseudo-single-domain (PSD) magnetite, which exsolved from pyroxenes and/or feldspars (Rajagopalan et al., 1993). The calculated remanence directions of the BHN vary depending on the method applied. A comparison of magnetization directions recovered by inversion, magnetic moment analysis, and paleomagnetic rock measurements for the BHN is presented from previous studies by MacLeod and Ellis (2013). Calculation of the remanence directions using convolutional neural networks as an alternative to inverse modeling was presented by Nurindrawati and Sun (2020). The remanence directions vary between 221° and 234° for declination and 6° and 20° for inclination. In general, these shallow inclinations indicate that the BHN intruded while at equatorial latitudes.

Previous optical and electron microscopy studies from the BHN have shown the presence of feldspars, pyroxenes, pyrite, magnetite, and ilmenite. Of the opaque minerals, magnetite has the greatest relevance to the modeled remanence directions. The magnetite is present as both discrete grains, and as lamellae within ilmenite grains. Electron microprobe work by Rajagopalan et al. (1995) confirmed the presence of randomly oriented fine-grained magnetite resulting in four populations. Demagnetization and hysteresis studies suggest two populations of SD magnetite with consistently different remanent directions due to secular variation during NRM acquisition, shape anisotropy, or magma flow (Rajagopalan et al., 1995). The shape anisotropy was interpreted to be due to exsolved

SD magnetite grains with defined crystallographic directions within host-silicates; however, this assumption was not confirmed. BHN samples carry a stable direction with only minor loss in NRM intensity with alternating field demagnetization up to 70 mT and a 50% loss by 120 mT. Room temperature hysteresis loops are dominated by multidomain (MD) magnetite and result in low bulk coercivity values. High magnetic susceptibility values measured by a magnetic susceptibility meter at surface range from 0.2 to 0.05 SI, similar to the susceptibility values of the paleomagnetic cores, which range from 0.023 to 0.087 SI.

The Black Hill Complex has not undergone later metamorphism and is only locally deformed. It is comprised of the Central (CNP), Cambrai (CMP), and the Black Hill (BHN) plutons, with lithologies from peridotites and troctolites to olivine gabbros and norites (Rajagopalan et al., 1993, 1995). The axes of the magnetic anomalies associated with the plutons have varying azimuths, which could reflect different bulk magnetization directions. The Central Pluton anomaly is parallel to the BHN anomaly and therefore would appear to have a similar remanence direction.

3. Materials and Methods

Specimen BH01A is from a core originally collected by Rajagopalan et al. (1993) in the northeast area of Black Hill (Figure 1). A polished thin section with a thickness of 30 μm is made from the sample. After acquiring the SMM scan, the distribution of opaque minerals in thin section are mapped using a Phenom XL scanning electron microscope (SEM) at the NTNU Rock Magnetic Laboratory. Pyroxene and plagioclase are the dominant silicates in the sample. A backscattered electron (BSE) image is made of the entire thin section to broadly map the sample mineral distribution. Higher resolution BSE images were made of individual oxide grains to map microstructures and major element mapping (Al, Ca, Fe, Mg, O, Si, Ti) is made to identify the opaque minerals, magnetite (mt - Fe_3O_4) and ilmenite (ilm— FeTiO_3), for post-modeling analysis. The ilmenite is present with and without reduction-exsolution lamellae of magnetite, where the lamellae vary in length from 3 to 50 μm . Based on BSE analysis, the orientation of the magnetite lamellae in ilmenite grains are at 70° and 330° degrees relative to the top of the sample. The dip of these lamellae below the surface cannot be assessed from BSE imagery and is therefore not considered for this study. The magnetite lamellae in ilmenite have a crystallographically controlled shape anisotropy (Robinson et al., 2016) and therefore, result in a preferred orientation. The paleomagnetic core from which the thin section is made has an anisotropy of magnetic susceptibility parameter ($P = K1/K3$) of 1.16. The

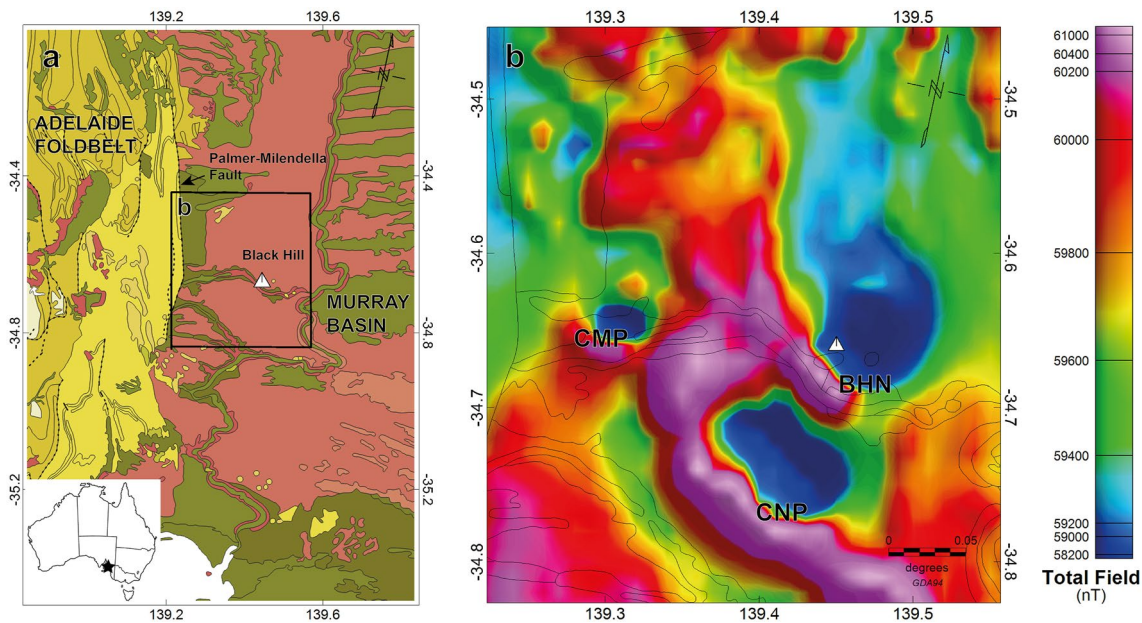


Figure 1. (a) Location of sample BH01A (white triangle) from Black Hill overlain on 1:1 000 000 surface geology and insert with approximate location within Australia (black star); the black box delimits the area shown in (b); (b) The sample was collected from the Black Hill Norite (BHN) Pluton (BHN), which has a prominent magnetic anomaly within a mapped mafic to intermediate intrusive rock (dolerite, norite, gabbro, diorite, microdiorite). The magnetic anomalies associated with the Central Pluton (CNP) and Cambrai Pluton (CMP) are also identified.

sample contains millimeter-to micron-sized grains, which are large compared to the thickness of the thin section (30 μ). This imposed geometry can result in strong shape anisotropy that could affect the magnetic response especially in MD magnetite grains. However, here, further evaluation of this effect is outside the scope of this paper.

Robinson et al. (2016) report the crystallographic relationships and orientation of magnetite lamellae in ilmenite from a companion BH01 specimen using transmission electron microscopy. The magnetite lamellae have very straight (001) boundaries and abrupt lamellar edges normal to (001). The authors discuss the potential magnetic effects along the (111)–(001) magnetite ilmenite lamellar contacts and the possible effect of strain on the contact boundaries of lamellae and host and suggest that these effects may enhance the coercivity of the magnetite lamellae.

The thin section of specimen BH01A is scanned using NTNU's Scanning Magnetic Microscope, SMM (Church & McEnroe, 2018). For mapping, the sample is placed in a Helmholtz coil to cancel out the local ambient magnetic field. Due to physical limitations of sensor-to-sample in scanning magnetometry, the SMM only measures the vertical component of the magnetic field (B_z). Lima and Weiss (2009) evaluated the measurement of a single component, B_z and concluded that it is sufficient to compute the remaining components, B_x and B_y . Because mapping is conducted in a near field-free environment, B_z ultimately maps the sample's magnetic remanence. Measurements are collected at 50 μ m increments in both the x and y directions. The SMM is a magnetic tunnel junction sensor which may generate a bias field from the currents that power the sensor. Based on instrument design, this field should be sufficiently low. The sensor also exhibits minor hardware noise, where vertical and horizontal striping occurred, with an average amplitude of 229 nT. The data set has a signal to noise ratio (SNR) of 18, which is sufficient for this analysis. This SNR is calculated by identifying the average amplitude (A_{noise}) of the noise and the amplitude of the average signal (A_{signal}) where

$$\text{SNR} = 20 \log_{10} \left(\frac{A_{\text{signal}}}{A_{\text{noise}}} \right)$$

The total magnetic moment of the thin section is measured in a cryogenic magnetometer at the Geological Survey of Norway and yielded a declination (D) of 351°, an inclination (I) of 3°, and a magnetic moment (m) of 4.5×10^{-7} Am².

Inversion is conducted using Tensor Research ModelVision software (Oldenburg & Pratt, 2007; Pratt et al., 2006). The software allows 3D modeling of magnetic anomaly sources and solves the nonlinear inverse problem using the Levenberg–Marquardt algorithm (Levenberg, 1944; Marquardt, 1963; Pastore et al., 2019, 2021), where the intensity, declination, and inclination vary independently. The software inversion procedure runs along multiple parallel profiles until the standardized residual error between the input/observed data, and modeled data are minimized along all profiles.

Magnetic data are modeled using the geomagnetic coordinate system convention with the x – y plane parallel to the sample surface and z (vertical intensity) negative downward and sensor elevation of 250 μ m used. All opaque minerals in the thin section are modeled using the multistep parametric inversion approach proposed by Pastore et al. (2019). Though silicates may contain magnetite particles, these are not modeled because the associated magnetic anomalies are below our selected threshold of 2,000 nT (~ 1.6 A/m). Each opaque grain is modeled as both a frustum and a compilation of small tabular arrays for a multi-scale analysis of the grain and highlighting microstructures. A frustum body is a single volume with prismatic shape to represent an entire grain. Tabular arrays are single cuboidal bodies with $n \times n$ dimensions in the map plane that represent smaller domains of the grain. In this case, the tabular arrays were 60 μ m \times 60 μ m. The tabular array dimensions are considered under sampled based on fundamental sampling methods in geophysical processing (Nyquist, 1928; Shannon, 1949) with a sampling interval of 50 μ m along both the x and y directions and there is a risk of aliasing. This is also an issue considering measurements were acquired at 250 μ m above the sample. However, as discussed by Pastore et al. (2021), the ideal modeling size of 100 μ m does not represent the mineralogical and microstructure variability that we intend to investigate here. The expectation is that tabular arrays will display heterogeneous properties of an ilmenite grain, which contains reduction-exsolution lamellae of magnetite e . The number of tabular arrays per grain depended on the size of the grain itself. Considering that the cuboidal tabular array will not perfectly fit within the irregularity of a typical grain boundary, the centroid of each tabular array must reside within the grain boundary to be included in the modeling. A model thickness of 30 μ m for all grains is used in both the frustum and tabular arrays based on the known thin section thickness. Therefore, each discrete body does not have an

infinite depth to bottom as commonly assumed in many magnetic calculations. Each body is assumed to have a vertical plunge. Considering the SMM sample spacing of 50 μm , opaque grains smaller than 100 μm are not modeled, though some of these grains have magnetizations that result in a magnetic anomaly.

In the ModelVision inversion process, the user can select the maximum number of iterations before the inversion is halted, the maximum free parameters, and target Root Mean Square Error (RMSE). The number of free parameters depends on the number of tabular arrays or frustums selected. For example, if two frustums are selected and the magnetization, declination, and inclination are free to vary in the inversion, this would result in six free parameters. The RMSE as implemented by the software is the root mean square difference between measured and calculated data, normalized by the measured data range from the SMM. Either the entire survey area or a subset area for the inversion can be selected. Because each survey station is considered a data point, the more data points and models selected for the inversion results in increased computation time. This means that tabular array inversion is more computationally intensive than the frustum modeling. Therefore, modeling for the tabular arrays is carried out on regions selected with the criteria of enclosing isolated groups of magnetic anomalies associated to large grains or multiple closely spaced grains. Typically, this is less than 600 free parameters (200 tabular arrays \times 3 variables of m , D , I) and 5,000 data points.

The software allows the user to select upper and lower bounds (tolerances) on magnetization intensity and direction in the inversion process and calculates the field response from bodies which are created in the 3D space. We run the inversion in multiple steps using the upper and lower bounds to limit the magnetization intensity range at each step, thus forcing the direction of the magnetization to be uniform in areas of uniform intensity. The magnetization direction can still vary at each step; however, the magnetization intensity can increase only gradually; this routine allows a more gradual change, which limits unrealistic spikes in the solution. Each frustum or tabular array is assigned to the laboratory measured total magnetization, declination, and inclination as an initial value. The directions are allowed to vary freely ($D = 0\text{--}360^\circ$, $I = \pm 90^\circ$) until the RMSE no longer varies by greater than 0.1%. The magnetization is then incremented in steps of 100 A/m in conjunction with the directions. Increments of 100 A/m may seem very coarse when modeling regional anomalies using aeromagnetic survey data. However, here, the interpretation deals with grain-sized sources which are small but intensely magnetized. Note that ModelVision conducts inversion modeling with an intensity (J) in A/m, but the measured magnetic field (B_z) acquired from the SMM is in nanoTeslas (nT). Therefore, any resultant magnetic anomaly maps presented here are plotted with scales in units of nT.

The inversion magnetization solutions are gridded in ModelVision using minimum curvature with a grid cell size of 60 μm . All subsequent grid math to produce residuals is conducted in Geosoft. Stereonets and rose diagrams are produced to assess the directional solutions and were made using Stereonet v.11 (Cardozo & Allmendinger, 2013).

For this initial stage of modeling, the opaque grains are considered compositionally homogeneous. Magnetic models are initially generated without knowing if these grains represent magnetite or ilmenite. Blind modeling is performed to assess whether ilmenite would be modeled with a remanent magnetization, and if so, to understand the circumstances under which this apparent magnetization arises.

4. Results

The SMM anomaly map (Figure 2) shows maximum amplitudes of $-15,458\text{--}14,971$ nT against background. Here, 103 grains are modeled, resulting in 103 frustums and 4,240 tabular array bodies. A RMSE average of 3.5% is achieved for frustum-modeled grains and 1.9% for tabular array-modeled grains. These averages are acceptable considering small-amplitude hardware noise associated with the SMM.

The magnetic anomalies from the SMM are co-registered with the BSE images from the SEM using three magnetic indicator grains to triangulate positioning, including a prominent magnetite grain along the top edge of the sample. Mapping the opaque grains is conducted by using the BSE image where each pixel of an opaque grain was allocated a value on whether it was ilmenite (1) or magnetite (0) (Figure 2, Figure S1 in Supporting Information S1). This identification method did not differentiate between ilmenite and ilmenite containing magnetite lamellae. Details of the classification of ilmenite and limitations in modeling are further discussed below. The frustum and tabular array bodies are then similarly assigned a value of ilmenite or magnetite based on the BSE image pixel classification to quantify typical magnetic properties of the two phases.

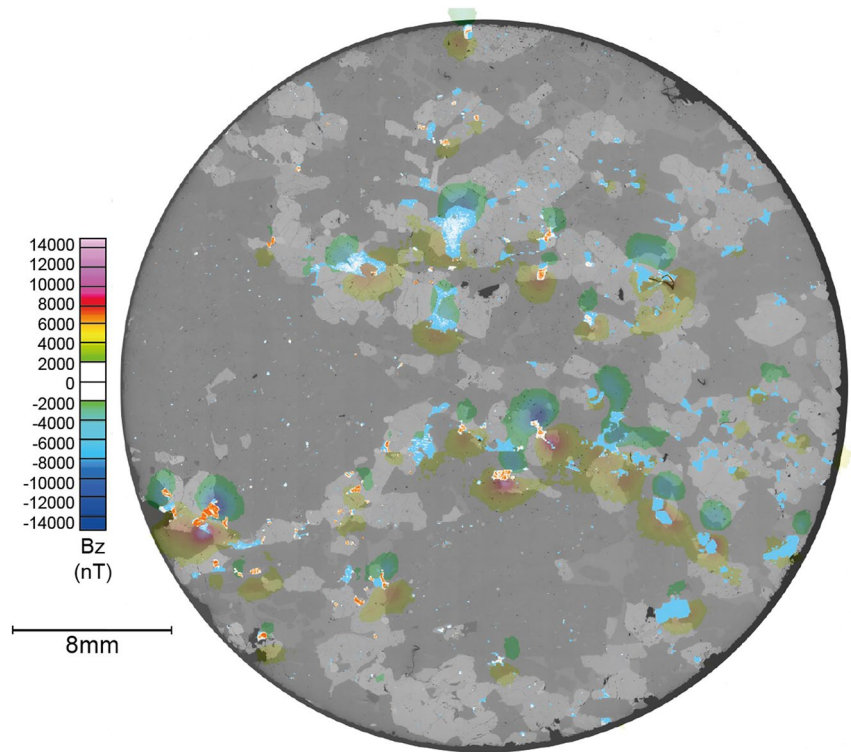


Figure 2. Backscattered electron (BSE) image of the thin section with magnetic field mapped by scanning magnetic microscopy. A range of $-2,000$ to $2,000$ nT has been omitted to highlight prominent anomalies and minimize background, which includes sensor noise. Opaque minerals have been automatically mapped as magnetite (orange) or ilmenite (blue) based on the BSE image.

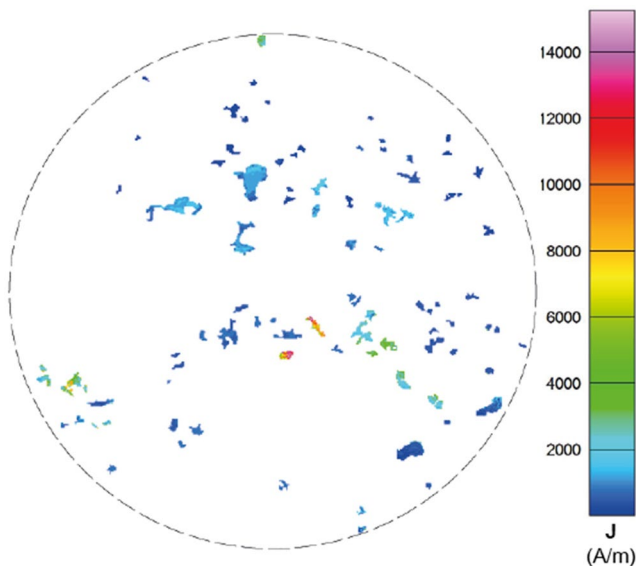


Figure 3. Calculated remanent intensity (J) for each tabular array, with warm colors indicating higher magnetization and cool colors indicating lower magnetization. Highest magnetization solutions result from two large, discrete magnetite grains in the center of the sample.

Modeled remanent intensity for the tabular arrays are shown in Figure 3 and the numerical results for inverted magnetization, declination and inclination are presented in Table 1. The magnetite grains are associated with the highest measured magnetic field values, and some ilmenite grains have coincident magnetic anomalies. The magnetite bodies are associated with higher modeled magnetizations relative to the ilmenite bodies shown in Figure 3. This is demonstrated in the statistics of the modeled grains (Table 1), where magnetite has an overall higher average magnetization ($J_{av} = 1989$ A/m), while ilmenite has lower average magnetization ($J_{av} = 934$ A/m). Considering that ilmenite is paramagnetic, the presence of magnetic anomalies and modeled magnetization indicates that some ilmenite grains in the sample may be associated with exsolved magnetite lamellae.

The modeled remanent inclinations and declinations for both magnetite and ilmenite are mapped on rose plots and stereonets for both frustum (Figure 4) and tabular array (Figure 5) geometries. Rose diagrams (a, b) use a bin size of 15% and petal lengths are % of the total population. The remanence directions are plotted on modified equatorial stereonets (Figure S2 in Supporting Information S1), where the small circles (latitudes) represent inclination ($\pm 90^\circ$), and the great circles (longitudes) represent the declination (0° – 360°). Separate stereonets are shown in Figures 4 and 5 for north-pointing (c, d) and south-pointing (e, f) declinations. Stereonets show Kamb contours in standard deviations (σ) and Bingham statistics, which include three eigenvalues (black squares) and

Table 1
Vector Averages for Inversion Model Solutions

	Declination, D_{av} (°)		Inclination, I_{av} (°)		Intensity, J_{av} (A/m)	
	F	T	F	T	F	T
Combined	347	354	12	10	523	1,338
Ilmenite*	351	354	2	4	341	934
Magnetite	347	354	16	13	688	1,989

Note. Comparison of inversion results between ilmenite and magnetite modeled grains for both frustum (F) and tabular (T) geometries. Declination and inclination results represent vector averages. Modeled directions are similar between both magnetite and ilmenite, indicating north-pointing, shallow vectors. There is a difference in modeled magnetization, which is expected considering ilmenite is paramagnetic and magnetite is ferrimagnetic. Modeled directions are similar between frustum and tabular array geometries; however, the intensity averages for frustum solutions are an order of magnitude lower than the tabular array solutions. *Includes ilmenite with and without microstructures.

the best fit great circle. The Kamb contouring distinguishes clusters (highest σ) and the Bingham statistics is a Principal Component Analysis to identify correlations.

For the frustum solutions, 98% of magnetite and 76% of ilmenite solutions plot in the northern half of the rose diagram (Figures 4a and 4b). The rose diagrams exhibit a maximum petal length for magnetite (Figure 4a, orange) of 19% between 331° and 345°, and for ilmenite (Figure 4b, blue) of 17% between 316° and 330°. These preferential directions in the ilmenite solutions are related to the crystallographically controlled exsolution of the magnetite lamellae in the ilmenite hosts. The north-pointing stereonet (Figures 4c and 4d) both exhibit single cluster solutions, which also correlate to the largest eigenvalue (1) of the Bingham statistics. For magnetite (Figure 4c), this cluster centers on an inclination of -18° and a declination of 345°. For ilmenite (Figure 4d), this cluster centers on an inclination of -4° and a declination of 348°. Meanwhile, the south-pointing stereonet (Figures 4e and 4f) show very few southward declinations, as also demonstrated in the rose diagrams. These few solutions are steeply inclined, bimodally distributed for both magnetite (Figure 4e) and ilmenite (Figure 4f). The results presented in these rose plots and stereonet are consistent with the total magnetic moment of the thin section measured on the cryogenic magnetometer and the statistics in Table 1 of north-pointing, shallow vectors.

For the tabular array, 89% of magnetite and 77% of ilmenite solutions plot in the northern half with very few solutions in the southern half of the rose diagram (Figures 5a and 5b). The rose diagrams exhibit a maximum petal length for magnetite (Figure 5a) of 12% between 346° and 360° and for ilmenite (Figure 5b) of 11% between 31° and 45°. Again, these directions are related to the crystallographically controlled magnetite lamellae in the ilmenite host grains, which are consistent with the AMS results. Several clusters are present in the stereonet of Figures 5c and 5d. These clusters can be traced back to specific grains. In the magnetite solutions, these clusters represent strongly magnetized discrete magnetite grains near the center of the sample. In the ilmenite solutions, these clusters are derived from the ilmenite grains (>1 mm), which contain numerous magnetite lamellae. Both south pointing stereonet (5e, 5f) show very steep inclinations, which are likely attributed to edge effects along the grain boundary in the inversion modeling (Figure S3 in Supporting Information S1). Again, the results presented in these rose plots and stereonet are consistent with the cryogenic measurements and statistics in Table 1, with predominantly north-pointing, shallow vectors.

Using the modeled remanent magnetizations and directions, the calculated total moment of the frustum bodies is $D = 356^\circ$, $I = 6.2^\circ$, $m = 2.2 \times 10^{-7} \text{ Am}^2$, while the total moment of the tabular array bodies is $D = 359^\circ$, $I = 8.3^\circ$, $m = 3.3 \times 10^{-7} \text{ Am}^2$. The moments calculated from the models are in the same order as the bulk moment measured in the cryogenic magnetometer, $m = 4.5 \times 10^{-7} \text{ Am}^2$. The modeled inversion directions are also close to the laboratory-measured declination of 351° and shallow inclination of 3°.

5. Classification of Ilmenite Grains

By combining the results of the modeled magnetization and directions with BSE images, an assessment of the mineralogy and microstructures can be carried out. This classification of ilmenite is important considering that it should be paramagnetic. However, numerous grains have been modeled with a remanent magnetization and direction.

Three ilmenite populations are identified in the thin section based on their modeled magnetization, microstructures (or lack thereof), and proximity to magnetite grains (Figure 6) and presented in Table 2: I—discrete paramagnetic ilmenite with no microstructures, II—ilmenite with reduction-exsolution lamellae of magnetite parallel to (001) of the host, and III—single phase oxy-exsolved ilmenite adjacent to a magnetite grain. The first ilmenite group solutions are associated with ilmenite grains lacking any microstructure and have no associated magnetic anomalies when using the <2,000 nT threshold. The second ilmenite group is associated with the magnetite lamellae. These are grains where the remanence direction may be influenced by the shape anisotropy of magnetite lamellae. Finally, the third ilmenite group is represented by ilmenite, which is oxy-exsolved from magnetite and is adjacent to magnetite grains.

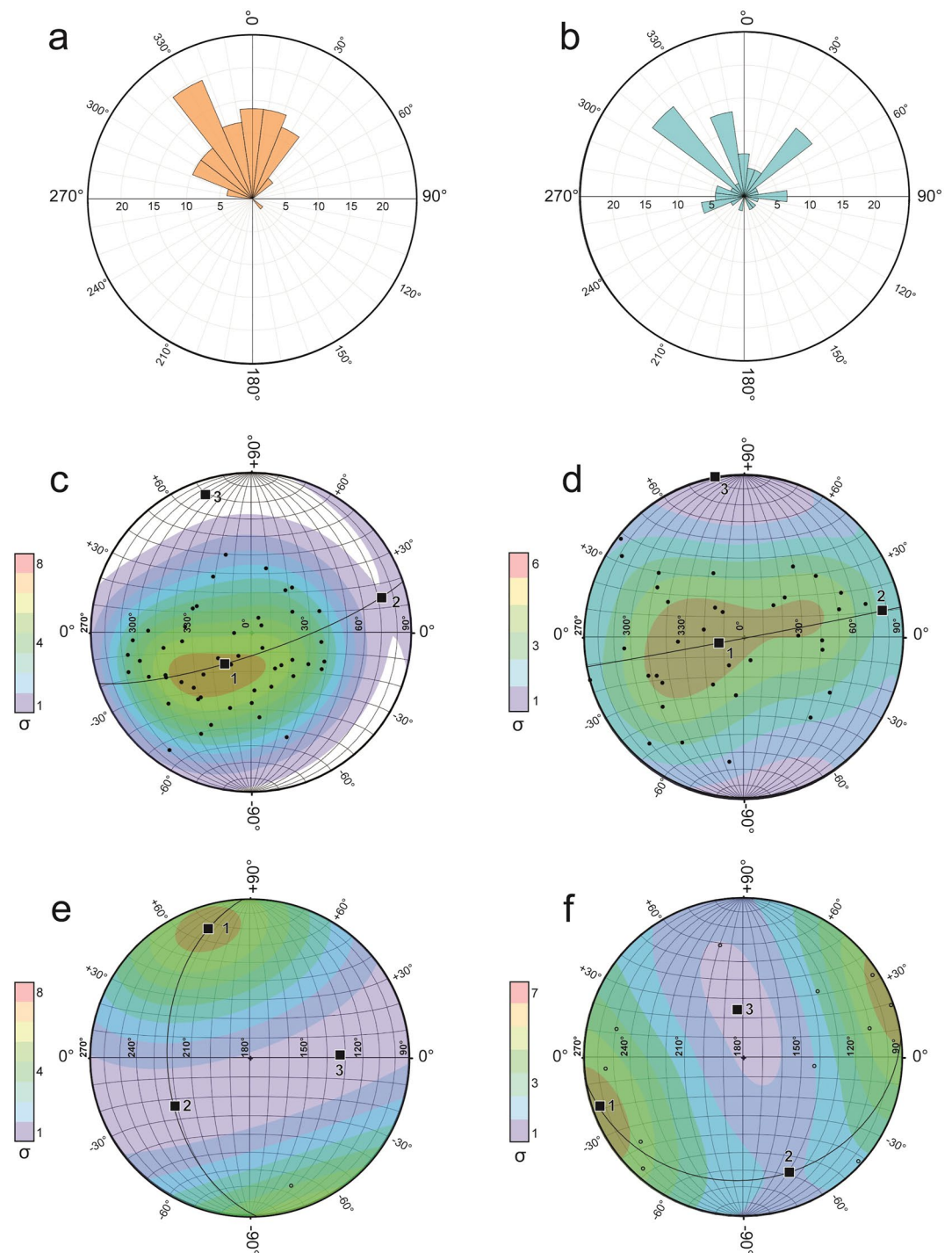


Figure 4. Rose diagrams (a, b) and stereonets (c–f) of the modeled magnetization of magnetite (left column) and ilmenite (right column) grains using frustum geometries. Rose diagrams use a bin size of 15% and petal lengths are % of population. The rose diagrams exhibit a maximum petal length for magnetite (a, orange) of 19% between 331° and 345°, and for ilmenite (b, blue) of 17% between 316° and 330°. The magnetite solutions are mostly contained to the northwest quadrant while the ilmenite solutions have three dominant directions, which result from the host ilmenite grains with magnetite lamellae along different orientations. Remanence inclination and declination are shown on modified equatorial stereonets, where the small circles represent inclination ($\pm 90^\circ$) and great circles represent declination. Separate stereonets are shown for the north-pointing (c, d) and south-pointing (e, f) declinations. All solutions are plotted in upper hemisphere. Stereonets show Kamb contours in standard deviations and Bingham eigenvalues (black squares) with best-fit great circle. The north pointing stereonets exhibit a single density of solutions; for magnetite (c) $I = -18^\circ$, $D = 345^\circ$ and for ilmenite (d) $I = -4^\circ$, $D = 348^\circ$. Meanwhile, the south pointing stereonets show steeply inclined bimodal distribution for both magnetite (e) and ilmenite (f).

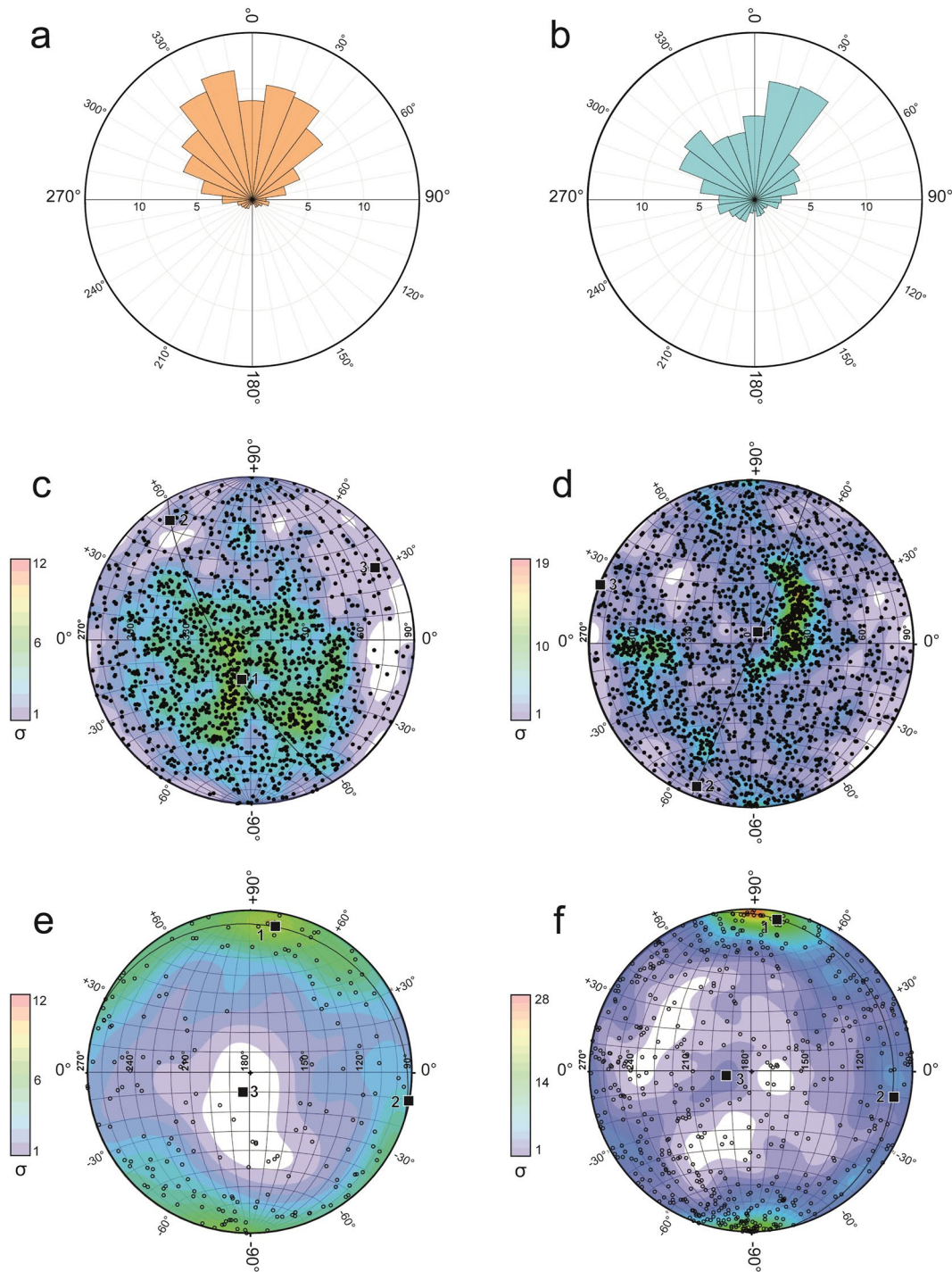


Figure 5. Rose diagrams (a, b) and stereonets (c–f) of the modeled magnetization of magnetite (left column) and ilmenite (right column) grains using tabular array geometries. Rose diagrams use a bin size of 15% and length of petals are % of population. Majority of solutions for both magnetite and ilmenite are in the northern half of the rose diagram. The rose diagrams exhibit a maximum petal length for magnetite (a, orange) of 12% between 346° and 360° and for ilmenite (b, blue) of 11% between 31° and 45° respectively. Remanence inclination and declination are shown on modified equatorial stereonets, where the small circles represent inclination ($\pm 90^\circ$) and great circles represent declination. Separate stereonets are shown for the north-pointing (c, d) and south-pointing (e, f) declinations. All solutions are plotted in upper hemisphere. Stereonets show Kamb contours in standard deviations and Bingham eigenvalues (black squares) with best-fit great circle. The north pointing stereonets (c, d) show several isolated clusters. For stereonet in c, these are highly magnetized, discrete magnetite grains near the center of the sample. For stereonet in d, these are ilmenite grains (>1 mm) with an abundance of magnetite lamellae. Both south pointing stereonets (e, f) show very steep inclinations, which are attributed to edge effects along the grain boundary in the inversion modeling.

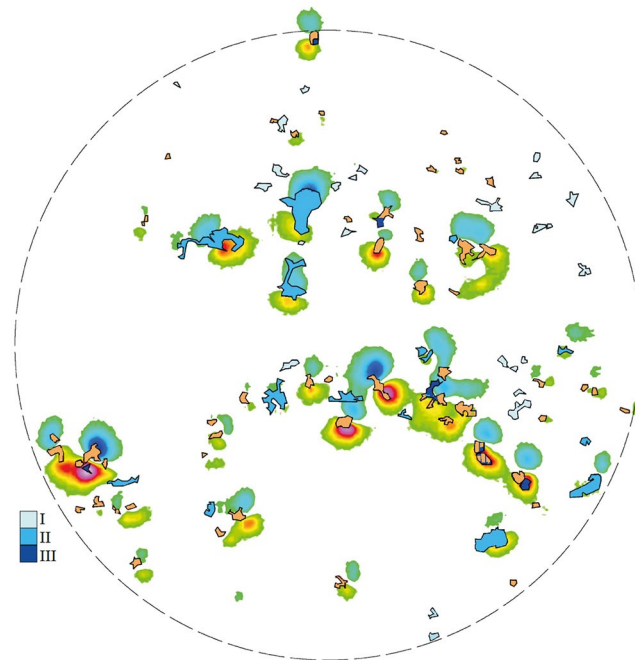


Figure 6. Classification of ilmenite grains (blues) based on impact by magnetite grains (orange): I—No impact; II—Ilmenite grain with magnetite lamellae; III—Ilmenite which is adjacent to a magnetite grain. The magnetic anomalies associated with small magnetite grains (less than 100 μm) are not modeled.

6. Inversion Results Over Selected Grains

Six grains are selected to better understand the relationship between magnetite and ilmenite for modeling (Figure 7). This subset of grains selected includes isolated ilmenite with magnetite blades (Figures 8 and 9) and composite grains of oxy-exsolved ilmenite with associated adjacent magnetite (Figures 10 and 11).

G1 and G2 are ilmenite grains containing magnetite lamellae (Figures 8 and 9). These isolated grains are the largest in the sample (2 mm \times 1 mm). When regarding the long axis of the lamellae relative to the thin section horizontal surface, they display different orientations within each grain; 70° for G1 and 330° for G2 relative to the top of the sample. Although previous studies (Robinson et al., 2016) have confirmed that the ilmenite have magnetite lamellae oriented along different crystallographic axes, the quantitative analysis of these lamellae cannot be made without further BSE or single-crystal axis measurements. Comparing Figures 8 and 9, the direction of the magnetite lamellae (parallel red bars) has an impact on the modeled declination of the ilmenite grains. The modeled magnetic directions will be dictated by the presence of the magnetite blades and their shape anisotropy since the host ilmenite is paramagnetic. Comparing the frustum and tabular array models (Table 3, G1 and G2), both types produced similar directions with minor differences (Δ) of $\Delta D = 4^\circ$ and $\Delta I = 2^\circ$. The magnetization for the frustums of G1 and G2 is approximately half of the calculated vector

Table 2
Ilmenite Inversion Solution Classifications

		Modeled intensity	Modeled direction
I	Discrete paramagnetic ilmenite	No magnetization	No direction
II	Ilmenite with magnetite blades	Modeled intensity value is higher than average (J_{av}), Table 1, due to magnetite lamellae	Modeled inclination and declination affected by the anisotropic magnetic susceptibility of the magnetite lamellae
III	Single phase oxy-exsolved ilmenite from magnetite	Modeled intensity value is higher than average (J_{av}), Table 1, due to adjoining magnetite	Modeled inclination and declination affected by adjoining magnetite

Note. General classification of modeled ilmenite grains. The three classifications represent grains that (I) have no influence from magnetite and those that are impacted by either (II) reduction-exsolution magnetite lamellae or (III) adjacent magnetite from which the ilmenite had oxy-exsolved from the original magnetite.

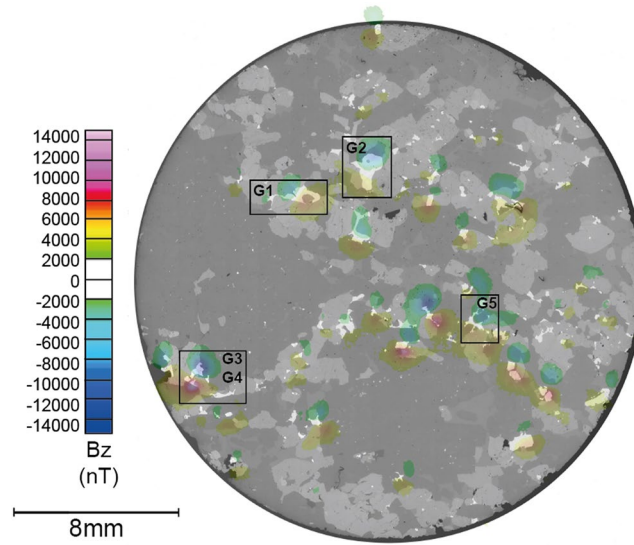


Figure 7. Backscattered electron image of thin section with magnetic field mapped by scanning magnetic microscopy. Four areas are selected to better understand the results and reliability of inversion modeling.

averaged magnetization of the tabular array G1 and G2 models. This suggests that frustum modeling smoothed magnetic variability across the grains.

Magnetite grains with oxidation-exsolution lamellae of ilmenite or areas where ilmenite is juxtaposed with magnetite grains are more complex areas for modeling because the anomalies generated by such geometries cannot be treated as isolated bodies. Typically, when magnetite is juxtaposed with ilmenite, the ilmenite is modeled with similar magnetic properties as the magnetite. In Figure 10, the ilmenite grain with magnetite blades (G3) is modeled with higher magnetization than the ilmenite magnetite average due to its proximity to large magnetite grains, compared to a similar ilmenite with magnetite blades grain (G4) in the bottom right of Figure 10. G3 has a J_{av} of 3651 A/m, while G4 has a J_{av} of 780 A/m (Table 3). Despite both grains having

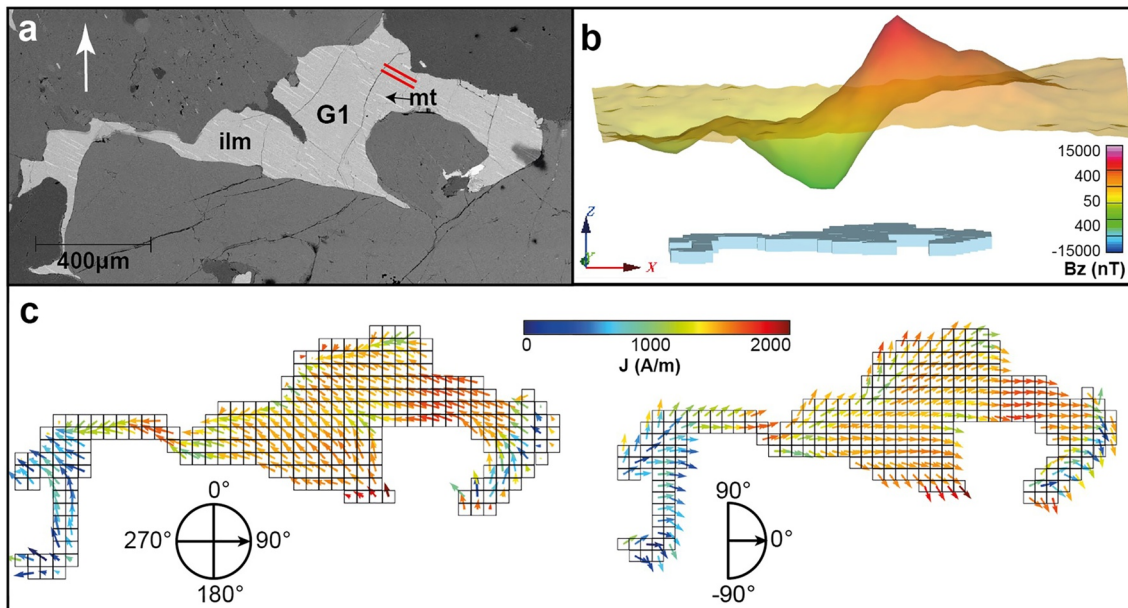


Figure 8. (a) Backscattered electron image of G1, ilmenite (ilm) with magnetite (mt). Lamellae azimuth indicated with double red lines. Top of grain indicated with white arrow; (b) 3D perspective of tabular array bodies and scanning magnetic microscopy grid (nT). (c) Calculated declination (left) and inclination (right) vectors are shown with a magnetization color-scale (J, A/m).

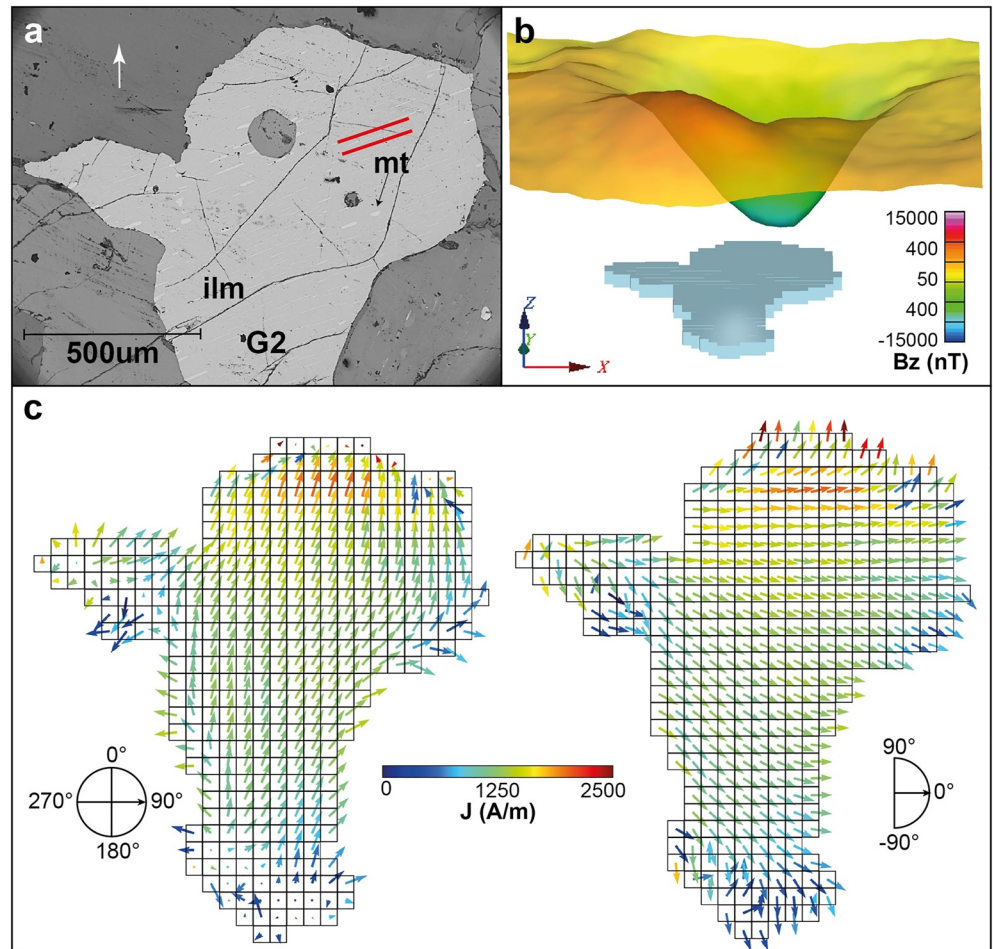


Figure 9. (a) Backscattered electron image of G2, ilmenite (ilm) with magnetite blades (mt). Lamellae azimuth indicated with double red lines. Top of grain indicated with white arrow; (b) 3D perspective of tabular array bodies and scanning magnetic microscopy grid (nT). (c) Calculated declination (left) and inclination (right) vectors are shown with a magnetization color-scale (J, A/m).

magnetite lamellae along 280° relative to the top, their modeled directions differ: $\Delta D = 10^\circ$ (F) to 15° (T) and G3 has a negative inclination, while G4 has a positive inclination (Figure 9b).

A composite grain, G5, shown in Figure 11 may be considered a combination of three separate grains—ilmenite with magnetite blades (ilm(e)), discrete ilmenite (ilm), and magnetite (mt). With the tabular array modeling, magnetic variation is mapped with lower magnetization of the ilmenite with and without lamellae (blues) versus the higher magnetization of the magnetite (greens) (Figures 11c and 11d). The ilmenite and magnetite solutions also exhibit variation in magnetic directions across the complex grain, with ilmenite having declinations closer to 0° than magnetite.

7. Discussion

Inspecting these grains in more detail suggests that there may be spurious solutions along the edge of the tabular array models. The concern for validity of results along sources edges and corners is expressed throughout potential field modeling and interpretation (e.g., depth-estimation routines), resulting in the development of methods to exclude erroneous solutions (Ugalde & Morris, 2010). In this work, all tabular bodies were created so that the centroid would be within the actual grain boundary and frustum boundary. However, considering that the inversion is performed over the entire volume of the tabular array, the solutions may not be representative. This may contribute to the cluster of steep solutions in Figure 5. G2 is selected to assess the validity of edge solutions considering it is a large grain with prominent directions due to magnetite lamellae, but also showed potential

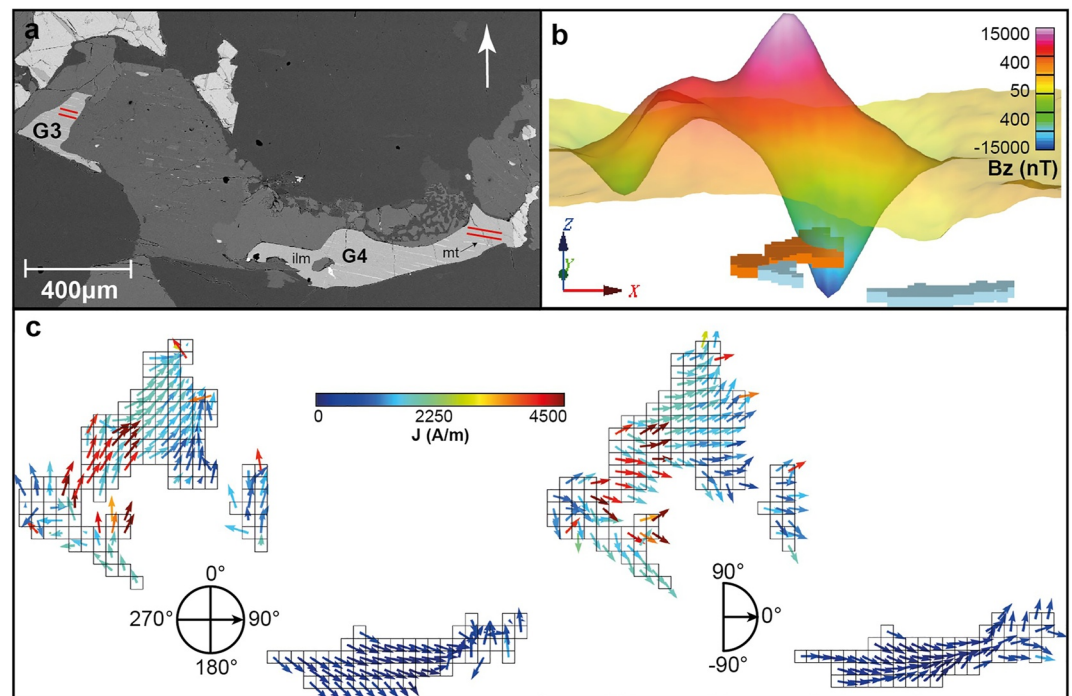


Figure 10. (a) Backscattered electron image of G3 and G4, which are ilmenite (ilm) grains with magnetite (mt) lamellae. Lamellae azimuth indicated with double red lines. Top of grain indicated with white arrow; (b) 3D perspective of tabular array bodies and scanning magnetic microscopy grid (nT); (c) Calculated declination (left) and inclination (right) vectors are shown with a magnetization color-scale (J, A/m).

spurious solutions along the grain boundary. All edge tabular bodies that extended beyond the grain boundary are removed and replaced with frustum bodies around the edge of the grain, so that they more closely represented the original grain. The results are shown in Table 4 and Figure S3 in Supporting Information S1. Analysis indicates a negligible difference between the original model and the new mixed model. In this case, if the edge solutions are artifacts, they have minimal impact on the overall analysis within the scope of this study.

Furthermore, the scale of modeling is important because it dictates what features can be accurately mapped and interpreted. Magnetic exploration is typically conducted at a regional meter-to-kilometer scale. However, here, we focus on the microscale. Grains are represented as both frustum bodies and tabular arrays to assess bulk characteristics versus microstructure variations. Comparing the resultant magnetic field grids (Figure S4 in Supporting Information S1) from both types of geometries with the original SMM measured magnetic field, the frustum has a difference of 120 ± 762 nT and the tabular grid had a difference of 119 ± 554 nT. This shows that the overall difference between the resultant grids is marginal. The largest variation occurs over large, discrete magnetite grains that have high amplitude anomalies.

To review the modeled fit with the measured magnetic field, a profile is selected over G2 (Figure 12). The tabular array profile over G2 shows a closer approximation of the measured profile than the frustum result. Returning to the stereonet in Figure 5, the tabular array solutions show more details, specifically with ilmenite grains with abundance of magnetite lamellae or highly magnetized discrete magnetite.

In general, the tabular array modeling results in a closer fit of the measured field than the frustum bodies. This is similar to the results shown in Pastore et al. (2021), where the vector average magnetization of the tabular models had an improved fit compared to frustum models. It is commonly assumed that the inversion with the greatest data matches or the inversion with the highest degrees of freedom produces the most reliable result. However, it has been shown in previous studies that this is not the case and may lead to a data misfit (Vital et al., 2019). In fact, there may be an optimal number of degrees of freedom, which vary depending on the source geometry, in this case study, the mineral size and shape. When selecting the number and type of geometry to construct the model, there is a balance between reducing tabular array size to best approximate

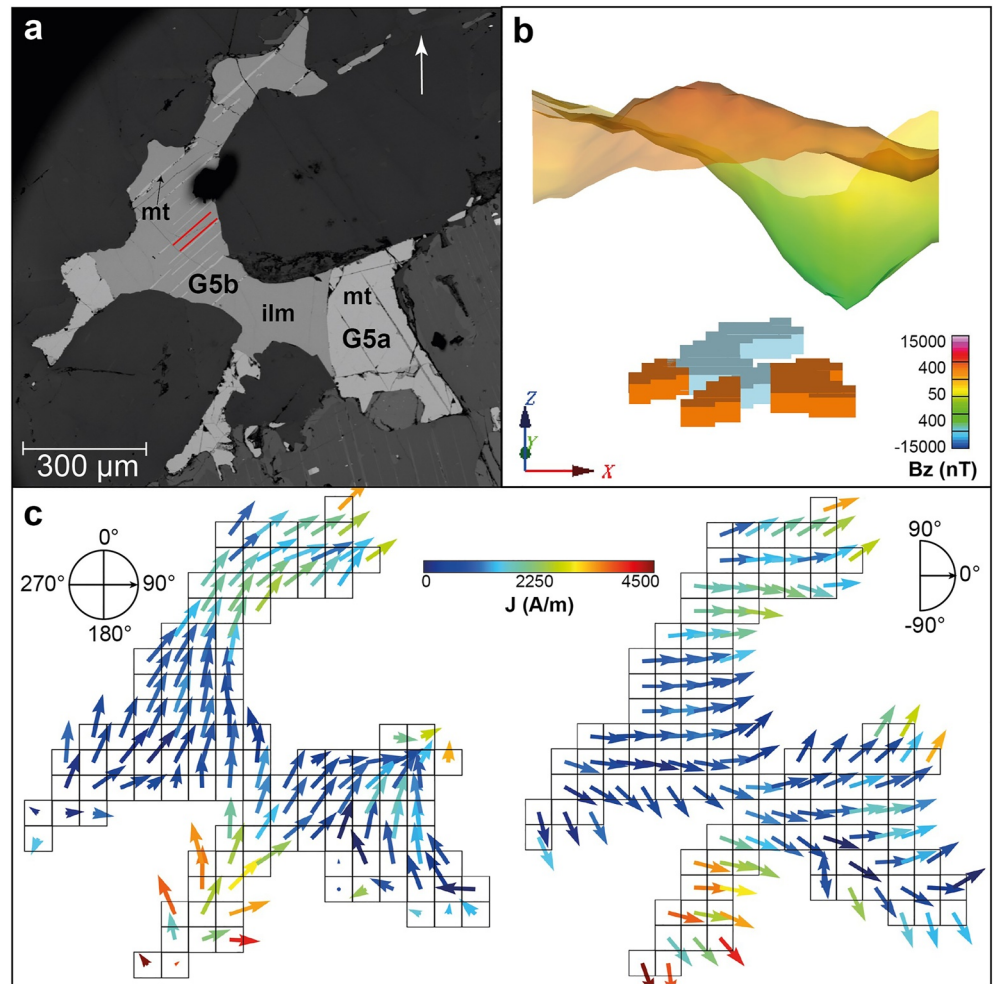


Figure 11. (a) Backscattered electron image of G5, which is a composite grain of G5a magnetite (mt) and G5b ilmenite (ilm) with magnetite lamellae. Lamellae azimuth indicated with double red lines. Top of grain indicated with white arrow; (b) 3D perspective of tabular array bodies and scanning magnetic microscopy grid (nT). (c) Calculated declination (left) and inclination (right) vectors are shown with a magnetization color-scale (J, A/m).

Table 3
Analysis of Inversion Solutions for Specific Grains

Grain	Declination, D_{av} (°)		Inclination, I_{av} (°)		Intensity, J_{av} (A/m)		Mineral
	F	T	F	T	F	T	
G1	296	300	5	7	608	1,395	ilm (e)
G2	74	70	-16	-19	544	1,314	ilm (e)
G3	353	352	14	-18	2,777	3,651	ilm (e)
G4	290	60	-11	22	144	780	ilm (e)
G5a	26	15	-8	-15	1,503	2,490	mt
G5b	35	30	12	3	1,264	2,338	ilm (e)

Note. Average vector results using data from frustum (F) and tabular (T) models for selected grains. Ilm (e) represents ilmenite with magnetite exsolution.

Table 4

Comparison of Original Models and New Mixed Model

Model	Magnetization (A/m)	Declination (°)	Inclination (°)
Original frustum	544	74	-16
Original tabular array	1,314	70	-19
Tabular array excluding edges	1,413	69	-18
Tabular + edge frustums	1,396	69	-18

Note. Average vector results for various models of G2, an ilmenite grain with magnetite lamellae. Evaluating these results, the impact of spurious edge solutions is negligible for this study. Refer to Figure S3 in Supporting Information S1 for mapped vector results.

the grain shape, while remaining large enough to avoid aliasing. Furthermore, if the tabular arrays are too large, edge effects become more apparent where tabular volumes at the edge of the grain shape do not accurately represent the grain, resulting in large directional artifacts or erroneous magnetizations. Therefore, depending on the SMM sampling rate and the size of the modeled tabular arrays, tabular arrays provide an opportunity to map localized variability within each grain that is otherwise averaged when modeled as a frustum body.

Finally, several assumptions are made in this magnetic modeling: The magnetic anomalies are independent and represented by a vertical-sided prism with a finite depth. There may also be small deviations in the co-registration of the SMM magnetic anomaly map with the backscatter electron image from the SEM. This is not an issue with regional maps where GPS coordinates can be used to align magnetic data with the ground. However, this is a common problem with borehole magnetics and thin-section mapping. Other laboratories are developing methodologies to mitigate this issue (Oda et al., 2016). However, the authors have found that grain triangulation remains one of the most reliable and repeatable methods.

ries are developing methodologies to mitigate this issue (Oda et al., 2016). However, the authors have found that grain triangulation remains one of the most reliable and repeatable methods.

8. Conclusions

Reliable micro-modeling is important not only because the measurements and interpretations at a regional scale of aeromagnetic data may be influenced by the summation of these small-scale anomalies but also

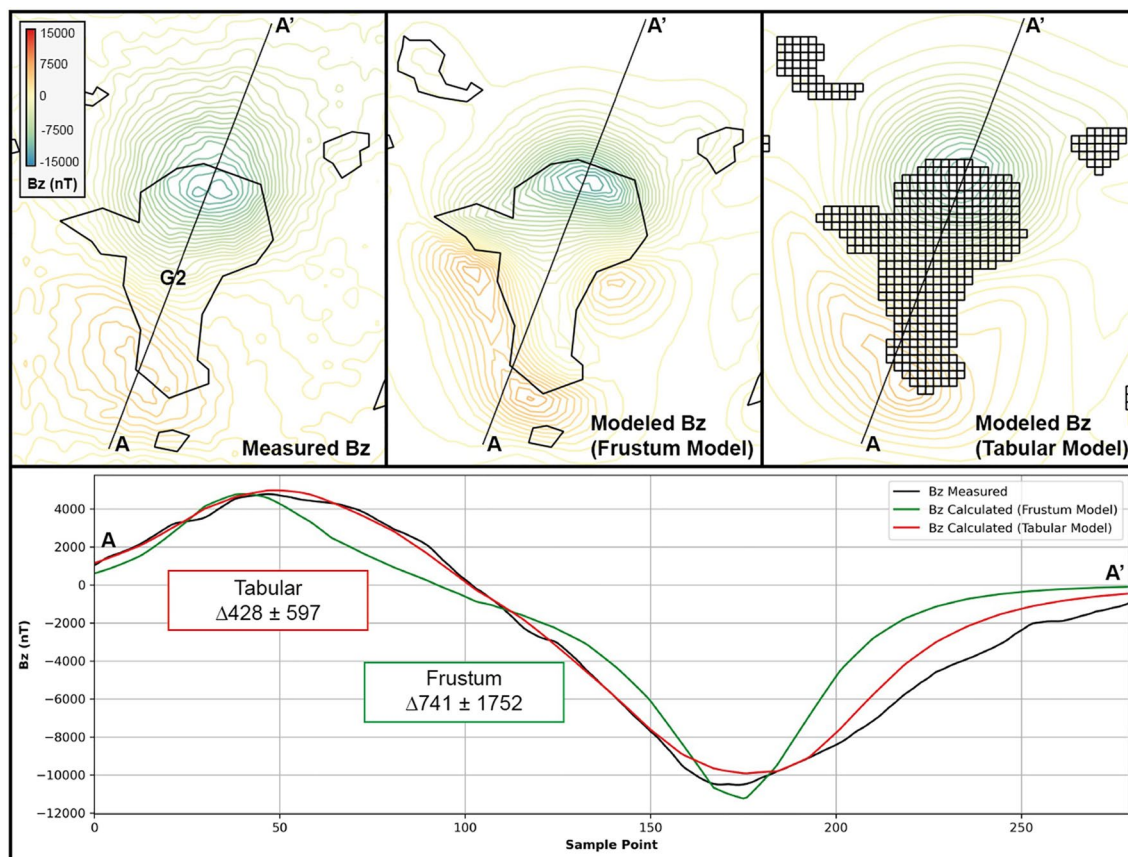


Figure 12. Comparison of measured and modeled profiles over an ilmenite grain with magnetite lamellae. To simplify figure contour legend is only shown on measured Bz, however, this is also the same for the modeled panels. The difference \pm standard deviation between measured and modeled profiles are shown in the green (frustum) and red (tabular array) boxes. The tabular array profile shows a closer fit to the measured Bz profile.

because of a deeper understanding of the magnetic sources at the grain scale. Here, microscale modeling was conducted on a thin section from the BHN, Australia. We showed that paramagnetic ilmenite may yield a magnetic signal in magnetic scans when host ilmenite grains contain magnetite lamellae, or when a magnetite grain contains large oxy-exsolved ilmenite lamella, which due to its size is modeled as an ilmenite body in tabular modeling.

Multiple remanent directions have been published through paleomagnetic measurements or through inversion modeling for the BHN area. In this study, the cryogenic laboratory measured magnetic moment of the thin section was $D = 351^\circ$, $I = 3^\circ$, and $m = 4.5 \times 10^{-7}$. Inversion modeling was conducted using data from NTNU's scanning magnetic microscope to map the NRM associated with grains and mineral assemblages within the thin section. The calculated total moment of the frustum modeling was $D = 356^\circ$, $I = 6.2^\circ$, $m = 2.2 \times 10^{-7} \text{ Am}^2$, while the total moment of the tabular array modeling was $D = 359^\circ$, $I = 8.3^\circ$, $m = 3.3 \times 10^{-7} \text{ Am}^2$. The observed and modeled magnetic moment values were on the same order of magnitude and orientation. The minor difference between the cryogenic measurement and the modeled values may be attributed to the discussed artifacts: edge solutions, aliasing, or minor sources not modeled.

Ilmenite grains were classified in one of three ways based on analysis of BSE images: (a) discrete paramagnetic ilmenite, (b) host ilmenite grains with magnetite lamellae, and (c) magnetite with oxy-exsolved ilmenite. Ilmenite containing magnetite lamellae were modeled with a magnetization intensity and the remanence direction was controlled by the blade shape anisotropy. Oxy-exsolved ilmenite lamellae larger than $100 \mu\text{m}$ were treated as individual grains, which were shown to be impacted by the adjacent magnetite. Ilmenite classified as 2 or 3 was modeled with a remanent intensity and skewed to an above-average value.

The scale of analysis was assessed with solutions from both frustum and tabular arrays on both overall modeled results and individual grains. Variability associated with mineralogy and microstructures was mapped using the tabular array models despite being considered under sampled by traditional methodology. These small-scale variations were averaged out in the frustum modeling, resulting in a lower over modeled magnetization. To minimize computation time, it is recommended to conduct frustum analysis for bulk modeling, which then can be used as a starting point for the tabular array modeling.

Data Availability Statement

Scanning magnetic microscopy data set for this research and all Supporting figures are available at <https://doi.org/10.18710/EOV6FB>.

Backscattered electron images (Figure S1 in Supporting Information S1); Simplified modified equatorial stereonet (Figure S2 in Supporting Information S1); Tabular array model compared with mixed model of G2 for solution artefacts (Figure S3 in Supporting Information S1); Residual grids of frustum versus tabular solutions (Figure S4 in Supporting Information S1) are provided in the Supporting Information S1 file. Inversions were conducted with ModelVision (2022) (Version 17.5) [Software] Tensor Research Pty Ltd. Figures were made with Oasis Montaj (2022) (Version 2021.2.1) [Software] Geosoft Inc. and Python using Spyder [Software] (Version 5.3.3) Python Software Foundation (Van Rossum & Drake, 1995). Stereonets and rose diagrams were made with Stereonet (2020) (Version 11) [Software] Richard W. Allmendinger © (Cardozo & Allmendinger, 2013).

References

- Austin, J. R., & Foss, C. A. (2014). The Paradox of Scale: Reconciling magnetic anomalies with rock magnetic properties for cost-effective mineral exploration. *Journal of Applied Geophysics*, *104*, 121–133. <https://doi.org/10.1016/j.jappgeo.2014.02.018>
- Balsley, J. B., & Buddington, A. F. (1958). Iron-titanium oxide minerals, rocks, and aeromagnetic anomalies of the Adirondack Area, New York. *Economic Geology*, *53*(7), 777–805. <https://doi.org/10.2113/gsecongeo.53.7.777>
- Bhattacharyya, B. (1966). Continuous spectrum of the total-magnetic-field anomaly due to a rectangular prismatic body. *Geophysics*, *31*(1), 97–121. <https://doi.org/10.1190/1.1439767>
- Biedermann, A. R., & McEnroe, S. A. (2017). Effects of magnetic anisotropy on total magnetic field anomalies. *Journal of Geophysical Research: Solid Earth*, *122*(11), 8628–8644. <https://doi.org/10.1002/2017jb014647>
- Brown, C., Tucker, D., & Anfiloff, V. (1988). An interpretation of the tectonostratigraphic framework of the Murray Basin region of southeastern Australia, based on an examination of airborne magnetic patterns. *Tectonophysics*, *154*(3–4), 309–333. [https://doi.org/10.1016/0040-1951\(88\)90110-2](https://doi.org/10.1016/0040-1951(88)90110-2)
- Cardozo, N., & Allmendinger, R. W. (2013). Spherical projections with OSXstereonet. *Computers & Geosciences*, *51*, 193–205. <https://doi.org/10.1016/j.cageo.2012.07.021>

Acknowledgments

This research was supported by the NTNU Faculty of Engineering at NTNU and the Research Council of Norway “Forskerprosjekt 2021—project number 324301.” The authors thank Bill Morris and an anonymous reviewer for their constructive revisions on scientific content and figure construction, and the Editor, Joshua Feinberg. The authors also thank Karl Fabian for the help in measurement on the cryogenic magnetometer at the Geological Survey of Norway.

- Church, N. S., & McEnroe, S. A. (2018). Magnetic field surveys of thin sections. In *ASEG extended abstracts* (pp. 1–5).
- Clark, D. A. (1997). Magnetic petrophysics and magnetic petrology: Aids to geological interpretation of magnetic surveys. *Journal of Australian Geology & Geophysics*, *17*(2), 83–103.
- Dunlop, D. J. (1981). The rock magnetism of fine particles. *Physics of the Earth and Planetary Interiors*, *26*(1–2), 1–26. [https://doi.org/10.1016/0031-9201\(81\)90093-5](https://doi.org/10.1016/0031-9201(81)90093-5)
- Egli, R., & Heller, F. (2000). High-resolution imaging using a high-Tc superconducting quantum interference device (SQUID) magnetometer. *Journal of Geophysical Research*, *105*(B11), 25709–25727. <https://doi.org/10.1029/2000JB900192>
- Foss, C., & McKenzie, B. (2011). Inversion of anomalies due to remanent magnetization: An example from the black hill norite of south Australia. *Australian Journal of Earth Sciences*, *58*(4), 391–405. <https://doi.org/10.1080/08120099.2011.581310>
- Grant, F. S. (1984). Aeromagnetism, geology and ore environments, I. Magnetite in igneous, sedimentary and metamorphic rocks: An overview. *Geoexploration*, *23*(3), 303–333. [https://doi.org/10.1016/0016-7142\(85\)90001-8](https://doi.org/10.1016/0016-7142(85)90001-8)
- Hankard, F., Gattacceca, J., Fermon, C., Pannetier-Lecoer, M., Langlais, B., Quesnel, Y., et al. (2009). Magnetic field microscopy of rock samples using a giant magnetoresistance-based scanning magnetometer. *Geochemistry, Geophysics, Geosystems*, *10*(10), Q10Y06. <https://doi.org/10.1029/2009GC002750>
- Levenberg, K. (1944). A method for the solution of certain non-linear problems in least squares. *Quarterly of Applied Mathematics*, *2*(2), 164–168. <https://doi.org/10.1090/qam/10666>
- Lima, E. A., & Weiss, B. P. (2009). Obtaining vector magnetic field maps from single-component measurements of geological samples. *Journal of Geophysical Research*, *11*(B6), B06102. <https://doi.org/10.1029/2008jb006006>
- MacLeod, I. N., & Ellis, R. G. (2013). Magnetic Inversion, a simple approach to the challenge of varying direction of rock magnetization. In *23rd international geophysical conference and exhibition*.
- Marquardt, D. (1963). An algorithm for least-squares estimation of nonlinear parameters. *Journal of the Society for Industrial and Applied Mathematics*, *11*(2), 431–441. <https://doi.org/10.1137/0111030>
- McEnroe, S. A., Fabian, K., Robinson, P., Gaina, C., & Brown, L. L. (2009). Crustal magnetism, lamellar magnetism and rocks that remember. *Elements*, *5*(4), 241–246. <https://doi.org/10.2113/gselements.5.4.241>
- ModelVision. (2022). ModelVision (2022) (Version 17.5) [Software]. Tensor Research Pty Ltd. <https://www.tensor-research.com.au/downloads>
- Nurindrawati, F., & Sun, J. (2020). Predicting magnetization directions using convolutional neural networks. *Journal of Geophysical Research*, *125*(10), e2020JB019675. <https://doi.org/10.1029/2020jb019675>
- Nyquist, H. (1928). Certain topics in telegraph transmission theory. *Transactions of the American Institute of Electrical Engineers*, *47*(2), 617–644. <https://doi.org/10.1109/t-aiee.1928.5055024>
- Oasis Montaj. (2022). Oasis Montaj (2022) (Version 2021.2.1). [Software]. Geosoft Inc. <https://my.seequent.com/products/oasis-montaj/latest>
- Oda, H., Kawai, J., Miyamoto, M., Miyagi, I., Sato, M., Noguchi, A., et al. (2016). Scanning SQUID microscope system for geological samples: System integration and initial evaluation. *Earth Planets and Space*, *68*(179), 179. <https://doi.org/10.1186/s40623-016-0549-3>
- Oldenburg, D. W., & Pratt, D. A. (2007). Geophysical inversion for mineral exploration: A decade of progress in theory and practice. *Proceedings of Exploration*, *7*(5), 61–95.
- Pastore, Z., Church, N., & McEnroe, S. A. (2019). Multistep parametric inversion of scanning magnetic microscopy data for modeling magnetization of multidomain magnetite. *Geochemistry, Geophysics, Geosystems*, *20*(11), 5334–5351. <https://doi.org/10.1029/2019gc008542>
- Pastore, Z., Lelievre, P., McEnroe, S. A., & Church, N. S. (2022). 3D joint inversion of scanning magnetic microscopy data. *Geophysical Research Letters*, *49*(1), e2021GL096072. <https://doi.org/10.1029/2021GL096072>
- Pastore, Z., McEnroe, S. A., Church, N. S., & Oda, H. (2021). Mapping and modeling sources of natural remanent magnetization in the microcline–Sillimanite Gneiss, Northwest Adirondack Mountains: Implications for crustal magnetism. *Geochemistry, Geophysics, Geosystems*, *22*(3), e2020GC009580. <https://doi.org/10.1029/2020gc009580>
- Phillips, J. D. (2005). Can we estimate magnetization directions from aeromagnetic data using Helbig's integrals? *Earth Planets and Space*, *57*(8), 681–689. <https://doi.org/10.1186/bf03351848>
- Pratt, D., McKenzie, K. B., & White, A. S. (2012). The remote determination of magnetic remanence. In *22nd international geophysical conference and exhibition*.
- Pratt, D. A., Foss, C. A., & Roberts, S. (2006). User guided inversion & visualisation of interpretation confidence. In *AESC conference*. Australian Earth Sciences Convention (AESC). Extended Abstract.
- Rajagopalan, S., Clark, D., & Schmidt, P. (1995). Magnetic mineralogy of the Black hill Norite and its aeromagnetic and palaeomagnetic implications. *Exploration Geophysics*, *26*(2–3), 215–220. <https://doi.org/10.1071/eg95215>
- Rajagopalan, S., Schmidt, P., & Clark, P. (1993). Rock magnetism and geophysical interpretation of the black hill norite, South Australia. *Exploration Geophysics*, *24*(2), 209–212. <https://doi.org/10.1071/eg993209>
- Robinson, P., Fabian, K., McEnroe, S., & Heidelberg, F. (2013). Influence of lattice-preferred orientation with respect to magnetizing field on intensity of remanent magnetization in polycrystalline hemo-ilmenite. *Geophysical Journal International*, *192*(2), 514–536. <https://doi.org/10.1093/gji/ggs046>
- Robinson, P., Harrison, R. J., & McEnroe, S. A. (2006). Fe²⁺/Fe³⁺ charge ordering in contact layers of lamellar magnetism: Bond valence arguments. *American Mineralogist*, *91*(1), 67–72. <https://doi.org/10.2138/am.2006.2012>
- Robinson, P., Heidelberg, F., Hirt, A. M., McEnroe, S. A., & Brown, L. L. (2006). Crystallographic–Magnetic correlations in single-crystal haemo-ilmenite: New evidence for lamellar magnetism. *Geophysical Journal International*, *165*(1), 431–31. <https://doi.org/10.1111/j.1365-246X.2006.02849.x>
- Robinson, P., McEnroe, S. A., Harrison, R. J., Fabian, K., Heidelberg, F., & Jackson, M. (2021). Lamellar magnetism and exchange bias in billion-year-old metamorphic titanohematite with nanoscale ilmenite exsolution lamellae—III. Atomic-Magnetic basis for experimental results. *Geophysical Journal International*, *226*(2), 1348–1367. <https://doi.org/10.1093/gji/ggab176>
- Robinson, P., McEnroe, S. A., Miyajima, N., Fabian, K., & Church, N. S. (2016). Remanent magnetization, magnetic coupling and interface ionic configurations of intergrown rhombohedral and cubic Fe-Ti oxides: A short survey. *American Mineralogist*, *101*(3), 518–530. <https://doi.org/10.2138/am-2016-5519>
- Robinson, R., Harrison, R. J., McEnroe, S. A., & Hargraves, R. (2002). Lamellar magnetism in the haemite-ilmenite series as an explanation for remanent magnetization. *Nature*, *418*(6897), 517–520. <https://doi.org/10.1038/nature00942>
- Roest, W. R., Verhoef, J., & Pilkington, M. (1992). Magnetic Interpretation Using 3-D Analytic Signal. *Geophysics*, *57*, 116–125. <https://doi.org/10.1190/1.1443174>
- Schmidt, P. W., Clark, D. A., & Rajagopalan, S. (1993). Early palaeozoic APWP of Gondwanaland: The delamerian revisited. *Exploration Geophysics*, *24*(2), 257–262. <https://doi.org/10.1071/eg93257>

- Shannon, C. E. (1949). Communication in the presence of noise. *Proceedings of the Institute of Radio Engineers*, 37(1), 10–21. <https://doi.org/10.1109/jrproc.1949.232969>
- Spector, A., & Grant, F. S. (1970). Statistical models for interpreting aeromagnetic models. *Geophysics*, 35(2), 293–302. <https://doi.org/10.1190/1.1440092>
- Stereonet. (2020). Stereonet (2020) (Version 11) [Software]. Richard W. Allmendinger © (Cardazo and Allmendinger, 2013). <http://www.geo.cornell.edu/geology/faculty/RWA/programs/>
- Thomas, I. M., Moyer, T. C., & Wikswo, J. P., Jr. (1992). High resolution magnetic susceptibility imaging of geological thin sections: Pilot study of a pyroclastic sample from the Bishop Tuff, California, U.S.A. *Geophysical Research Letters*, 19(21), 2139–2142. <https://doi.org/10.1029/92GL02322>
- Ugalde, H., & Morris, W. A. (2010). Cluster analysis of Euler deconvolution solutions: New filtering techniques and geologic strike determination. *Geophysics*, 75(3), 61–70. <https://doi.org/10.1190/1.3429997>
- Van Rossum, G., & Drake, F. L., Jr. (1995). *Python reference manual*. Centrum voor Wiskunde en Informatica Amsterdam.
- Vital, L. B., Foss, C., Oliviera, V. C., Jr., & Barbosa, V. (2019). Magnetic Field Inversion—The cost of freedom. In *AEGC 2019*. <https://doi.org/10.1080/22020586.2019.12073182>
- Weiss, B. P., Kirschvink, J. L., Baudenbacher, F. J., Vali, H., Peters, N. T., Macdonald, F. A., & Wikswo, J. P. (2000). A low temperature transfer of ALH84001 from Mars to Earth. *Science*, 290(5492), 791–795. <https://doi.org/10.1126/science.290.5492.791>
- Weiss, B. P., Lima, E. A., Fong, L. E., & Baudenbacher, F. J. (2007). Paleomagnetic analysis using SQUID microscopy. *Journal of Geophysical Research*, 112(B9), B09105. <https://doi.org/10.1029/2007JB004940>